

# Investigation into Lithium-Ion Conductivity and Redox Stability of Selenium-Doped Lithium Lanthanum Titanate

by

Lambert Hu

Submitted to the  
Department of Mechanical Engineering  
in Partial Fulfillment of the Requirements for the Degree of

Bachelor of Science in Mechanical Engineering

at the

Massachusetts Institute of Technology

June 2023

©2023 Lambert Hu. All rights reserved.

The author hereby grants to MIT a nonexclusive, worldwide, irrevocable,  
royalty-free license to exercise any and all rights under copyright,  
including to reproduce, preserve, distribute, and publicly display copies of  
the thesis, or release the thesis under an open-access license.

Authored by: Lambert Hu

Department of Mechanical Engineering

May 12, 2023

Certified by: Yang Shao-Horn

JR East Professor of Engineering

Thesis Supervisor

Accepted by: Kenneth Kamrin

Associate Professor of Mechanical Engineering

Undergraduate Officer

# Investigation into Lithium-Ion Conductivity and Redox Stability of Selenium-Doped Lithium Lanthanum Titanate

by

Lambert Hu

Submitted to the Department of Mechanical Engineering  
on May 12, 2023 in Partial Fulfillment of the  
Requirements for the Degree of

Bachelor of Science in Mechanical Engineering

## ABSTRACT

Selenium-doped lithium lanthanum titanate of composition  $\text{Li}_{0.33}\text{La}_{0.56}\text{Ti}_{1-x}\text{Se}_x\text{O}_3$  ( $x = 0, 0.025, 0.050, 0.075$ ) was attempted using a two-step conventional synthesis process to investigate the potential of the material as a solid-state electrolyte in lithium-ion batteries. Impedance spectroscopy data yielded a maximum room temperature bulk conductivity of  $(1.73 \pm 0.10) \times 10^{-3} \text{ S cm}^{-1}$  ( $E_{\text{Bulk}} = 0.35 \pm 0.03 \text{ eV}$ ) and grain boundary conductivity of  $(1.20 \pm 0.10) \times 10^{-4} \text{ S cm}^{-1}$  ( $E_{\text{GB}} = 0.37 \pm 0.01 \text{ eV}$ ) for nominal composition  $x = 0.050$ . Preliminary stability measurements through three-electrode cyclic voltammetry suggests potential for LLTO stabilization against Li metal anode through further selenium substitution. However, further work is required to confirm the exact elemental composition of selenium-doped samples.

Thesis Supervisor: Yang Shao-Horn

Title: JR East Professor of Engineering

## **Acknowledgements**

I would like to first express my gratitude to my academic advisor and thesis supervisor, Professor Yang Shao-Horn, who welcomed me into her lab and who has offered her invaluable guidance throughout my journey as a mechanical engineering undergraduate. I would also like to offer a heart-felt thank you to graduate student Daniele Vivona and post-doc Bryce Tappan for their support and encouragement during my time with the MIT Electrochemical Energy Lab and especially over the course of my final semester at MIT. This project would also not have been possible without the generous help of graduate student Daniel Wang, who helped me to sputter my pellets with gold; graduate student Gregoire Heller, who first taught me how to analyze EIS data; and post-doc Yaolin Xu, who taught me how to assemble a three-electrode set-up for CV.

## **Table of Contents**

<b>Abstract</b>	2
<b>Acknowledgements</b>	3
<b>Table of Contents</b>	4
<b>List of Figures</b>	5
<b>List of Tables</b>	6
<b>1. Introduction</b>	7
<b>2. Method</b>	9
2.1 Sample Synthesis	9
2.2 Characterization Techniques – Powder X-Ray Diffraction	9
2.3 Characterization Techniques – Electrochemical Impedance Spectroscopy	10
2.4 Characterization Techniques – Cyclic Voltammetry	11
<b>3. Results and Discussion</b>	12
3.1 X-Ray Diffraction Analysis	12
3.2 Obtaining Bulk and Grain Boundary Conductivity Values	14
3.3 Bulk and Grain Boundary Conductivity Comparison	19
3.4 Stability of Se-Doped LLTO	21
<b>4. Conclusion</b>	23
<b>5. References</b>	25
<b>6. Appendices</b>	27

## List of Figures

<b>Figure 1:</b> Comparison of RT impedance data obtained from SP-300 and VMP3 potentiostats	10
<b>Figure 2:</b> Diagram of three-electrode test cell with partially assembled top view	11
<b>Figure 3:</b> Background subtracted XRD spectra of Se-doped LLTO samples	12
<b>Figure 4:</b> Comparison of sample lattice parameters with nominal Se content	14
<b>Figure 5:</b> Comparison of RT impedance plots for bulk and grain boundary semicircles	15
<b>Figure 6:</b> Representative image of high-temperature impedance data fitting	16
<b>Figure 7:</b> Representative image of low-temperature impedance data fitting	17
<b>Figure 8:</b> Arrhenius plots from bulk and grain boundary conductivity data	18
<b>Figure 9:</b> RT bulk and grain boundary conductivity values for Se-doped LLTO	19
<b>Figure 10:</b> Voltammograms of undoped and 5% Se-doped LLTO sample (1.0-2.8V vs. Li)	21
<b>Figure 11:</b> Image of 5% Se-doped LLTO pellet after accidental contact with lithium foil	23

## **List of Tables**

<b>Table 1:</b> Lattice constant values from Rietveld refinement of LLTO sample XRD spectra	13
<b>Table 2:</b> Ionic conductivity data and activation energy data of Se-doped LLTO	19
<b>Table 3:</b> Caliper measured dimensions of pellets used for impedance spectroscopy	27

# 1. Introduction

Owing to desirable properties such as high energy density and long cycle life, lithium-ion battery technology has been employed in a wide variety of applications, from portable electronic devices to electric vehicles [1]. However, the current use of liquid electrolytes - which consist of a lithium salt dissolved in a solution of organic solvents – has led to safety concerns related to the thermal stability of the organic solvents and the health and environmental hazard posed by battery leakage [2]. Improvements to the energy density of lithium-ion batteries will also be important in light of efforts towards decarbonizing the energy system while still addressing growing global energy demands. Although lithium metal anodes have very low redox potential ( $-3.040\text{V}$  vs. standard hydrogen electrode) and could enable higher energy densities, exploration and implementation in lithium metal batteries have been stymied by safety issues due to the growth of lithium dendrites during the cycling of lithium-metal liquid electrolyte cells, which can lead to short-circuiting and the cell exploding [3].

Inorganic solid-state electrolytes are a promising alternative that can address the safety issues of thermal stability and leakage that stem from the organic solvents used in liquid electrolyte batteries. Although lithium dendrites can also form in solid-state electrolyte cells, the often higher modulus of such ceramic materials can, in principle, slow the detrimental propagation of dendrites through the system [4]. It should be noted that an ideal electrolyte must also exhibit a high ionic conductivity and remain stable against the electrodes employed. On the former consideration, the perovskite-type lithium lanthanum titanate (LLTO) – a series of compounds of the formula  $\text{Li}_{3x}\text{La}_{(2/3-x)}\text{TiO}_3$  ( $0.04 < x < 0.16$ ) – exhibits a fairly high ionic conductivity that approaches those of liquid electrolytes. Notably, at room temperature the composition  $\text{Li}_{0.33}\text{La}_{0.56}\text{TiO}_3$  ( $x = 0.11$ ) exhibits the maximum bulk lithium-ion conductivity of the series at  $1 \times 10^{-3} \text{ S/cm}$ , which is only an order of magnitude below commercially employed liquid electrolytes [1]. On the latter consideration for stability with the electrodes, however, LLTO has been found to rapidly reduce when in contact with lithium metal anodes [5], which increases its electronic conductivity and leads to short-circuiting.

A common strategy towards improving the ionic conductivity of LLTO, which might also prove useful towards addressing the material's stability against lithium metal anodes, is to introduce dopants into the  $\text{ABO}_3$  perovskite structure. The  $\text{Ti}^{4+}$  on the octahedral B-site is of

particular interest as  $d^0$  cations, i.e., transition metal ions without valence electrons in their outermost d-orbital, are readily reduced [6]. Because the reduction of  $Ti^{4+}$  to  $Ti^{3+}$  has been attributed to the rise in electronic conductivity seen in LLTO against lithium metal anodes [1], the partial or complete replacement of the B-site  $Ti^{4+}$  could be a strategy to improve the stability of LLTO. While the use of  $Te^{6+}$  for the B-site of a lithium-rich perovskite model ( $Li_{1.5}La_{1.5}TeO_6$ ) was found to result in a redox stable material when cycled against lithium metal anode down to 0.1V vs. Li, the reported ionic conductivity was  $5.8 \times 10^{-5} \text{ S cm}^{-1}$  [7]. This is more than two orders of magnitude lower than that of commercially employed liquid electrolytes ( $\sim 1 \times 10^{-2} \text{ S cm}^{-1}$  [8]).

A previously published effort at doping the B-site of LLTO with isovalent transition metal cations [9] identified the dopant ionic radius as a potential factor on changes to ionic conductivity: smaller ionic radii could shorten and therefore strengthen the B-O bond at the expense of the A-O bond. As lithium ions occupy A-site vacancies [1], the weakening of the A-O bond would thus increase lithium ion mobility, which might in turn increase ionic conductivity. Looking one row above tellurium, VI-coordinated  $Se^{4+}$  has an effective ionic radius of 0.50Å, which is smaller than that of VI-coordinated  $Ti^{4+}$  (0.605Å) or  $Te^{4+}$  (0.97Å) [10]. As selenium has similar oxidation states and associated coordination numbers to tellurium - lacking a 3+ oxidation state unlike titanium - this study sought to investigate the effect of partial  $Se^{4+}$  B-site doping on the ionic conductivity and redox stability of lithium lanthanum titanate with a lithium metal anode. The aim of the endeavor is to expand upon the extensive body of doped-LLTO literature, which, to the author's knowledge, has focused on transition metal substitutions for B-site doping. Because the LLTO series member  $Li_{0.33}La_{0.56}TiO_3$  was found to have the largest bulk ionic conductivity at room temperature [11], this material was chosen as the base for doping to produce samples of nominal composition  $Li_{0.33}La_{0.56}Ti_{1-x}Se_xO_3$  ( $x = 0, 0.025, 0.050, 0.075$ ). The goal was to optimize the Se-content to improve the electrochemical stability of LLTO against a Li metal anode while maintaining or improving ionic conductivity to a comparable value to those seen in commercial liquid electrolytes.



## 2. Method

### 2.1 Sample Synthesis

Samples of  $\text{Li}_{0.33}\text{La}_{0.56}\text{Ti}_{1-x}\text{Se}_x\text{O}_3$  ( $x = 0, 0.025, 0.050, 0.075$ ) were prepared using a two-step solid-state synthesis procedure similar to one reported elsewhere [12]. Stoichiometric amounts of  $\text{La}_2\text{O}_3$  ( $\geq 99.9\%$  Aldrich Chem.),  $\text{TiO}_2$  ( $\geq 99.7\%$  Aldrich Chem.), and  $\text{SeO}_2$  (99.8% Acros Organics) were mixed with 10 weight% excess  $\text{Li}_2\text{CO}_3$  ( $\geq 99.0\%$  Sigma-Aldrich) with an agate mortar under a fume hood for 20 minutes. The excess lithium carbonate was added to compensate for lithium evaporation during synthesis. For the first step of the process, the homogenized precursor powder was calcined in a covered alumina crucible under  $\text{O}_2$  flow at  $1000^\circ\text{C}$  for 12 hours.

For the second step, a portion of the calcined powder was weighed out and lightly ground with 5 weight% polyvinyl butyral (PVB) as binder for 10 minutes. To promote mixing between the powder and binder, several drops of ethanol were added to the precursor-PVB mixture to create a slurry, which was allowed to dry before being reground for 20 minutes. The binder-containing powder was pressed at 5 metric tons to produce cylindrical 0.5g pellets. The pellets were then laid on a bed of binder-free mother powder in an alumina crucible, covered with more of the same mother powder, and then sintered under  $\text{O}_2$  flow at  $1150^\circ\text{C}$  for 12 hours. The alumina crucible was again covered with its lid. A ramp rate of  $3^\circ\text{C}$  per min was used for all heating and cooling steps.

### 2.2 Characterization Techniques – Powder X-Ray Diffraction

To identify phases and characterize the structure of the prepared samples, a sintered pellet for each composition was ground back into powder. Powder X-ray diffraction (XRD) spectra were then acquired at room temperature using a Bruker D2 PHASER diffractometer with LYNXEYE XE-T linear detector,  $\text{Cu K}\alpha$  radiation, and the Bruker DIFFRAC.SUITE software. XRD patterns were obtained through one-hour continuous scans that swept between  $2\theta$  values of 15 to 90 degrees. Crystal phase candidates were first identified using HighScore Plus; afterwards, Rietveld refinements were carried out using TOPAS to identify peaks and obtain lattice parameters.

## 2.3 Characterization Techniques – Electrochemical Impedance Spectroscopy

To obtain bulk and grain boundary lithium ionic conductivities, symmetric cells were prepared by DC-sputtering Au electrodes (60 nm thick) on both sides of the LLTO pellets ( $\approx 1.5$  mm thickness and  $\approx 9$  mm diameter, see Appendix A). Because the high-frequency semi-circle, which corresponds to bulk conductivity [13], tended to partially or completely disappear above room temperature, especially for the Se-doped samples, two separate heat-chamber mediated AC impedance methods were employed. For the bulk conductivity, impedance measurements were made using a Biologic SP-300 Potentiostat over a frequency range of 1 Hz to 7 MHz and temperature range of 263.15 K to 298.15 K (room temperature). Because conductivity has been found to exhibit Arrhenius behavior, the low temperature range increased the size and visibility of the high-frequency semi-circle within the range of the SP-300 potentiostat (max freq. 7 MHz).

For the grain boundary, impedances were measured using a Biologic VMP3 Multichannel Potentiostat over a frequency range of 1 Hz to 1 MHz and temperature range of 303.15 K to 353.15 K. In both methods, an EL-CELL ECC-Combi test cell was used, and data was collected by the EC-Lab program. For the grain boundary, high-temperature wire connected the test cell to the potentiostat. As there appeared to be good agreement between room temperature impedance data obtained from the two devices for the same pellet (Fig. 1), data from the two potentiostats were considered to be comparable and analyzed using the ZView4 program.

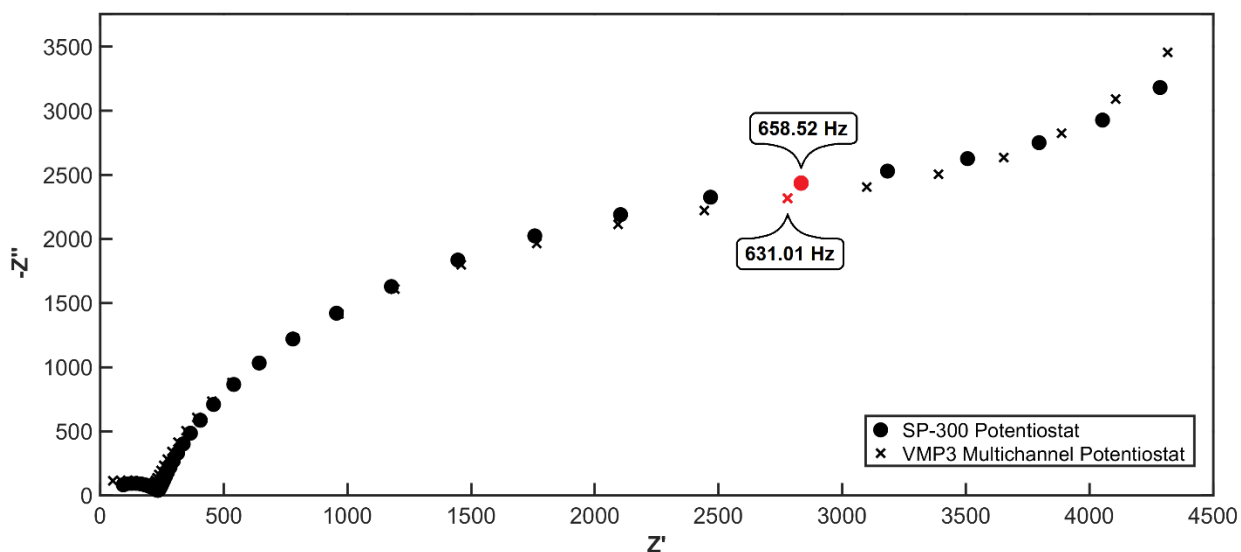


**Figure 1.** Comparison of room temperature impedance data obtained from SP-300 and VMP3 Multichannel Potentiostat for a pellet of composition  $\text{Li}_{0.33}\text{La}_{0.56}\text{Ti}_{0.975}\text{Se}_{0.025}\text{O}_3$  ( $x = 2.5$ )

## 2.4 Characterization Techniques - Cyclic Voltammetry

Cyclic voltammetry (CV) measurements were conducted with a Biologic VMP3 Multichannel Potentiostat and the EC-Lab program using a three-electrode EL-CELL ECC-Combi test cell set-up (Fig. 2a). Asymmetric cells (Au | LLTO | Separator | Li) were assembled with a sputtered Au electrode (60 nm thick) on one face as the working electrode. On the other side, an approximately 12mm diameter circular piece of Celgard PP membrane separated the solid-state electrolyte (SSE) pellet from a 6mm diameter piece of lithium metal foil, which served as the counter electrode. 20  $\mu\text{L}$  of 1.0 M  $\text{LiPF}_6$  in EC/DEC = 50/50 (v/v) was added to the separator as the liquid electrolyte connection. The asymmetric cell was separated from the reference lithium metal foil using a stainless-steel spacer nestled within a  $\approx 1.5$  cm PTFE ring (Fig. 2b). A ring of glass fiber was then looped around the PTFE ring, to which was added 50  $\mu\text{L}$  of the same liquid electrolyte used with the polymer membrane separator. The reference lithium foil was loaded into the test cell at the final step of assembly using an EL-CELL ECC-RefLoad tool.

Because LLTO was found to reduce at and below a potential of 1.8V vs. Li [14], CV for a pellet of S00 and S50 were obtained using a voltage range of 1.0V to 2.8V vs. Li to compare the stability window of the selenium-doped sample against a lithium metal anode. A scan rate of 0.1  $\text{mV s}^{-1}$  was employed. The test cell was left to equilibrate for four hours before each experiment.

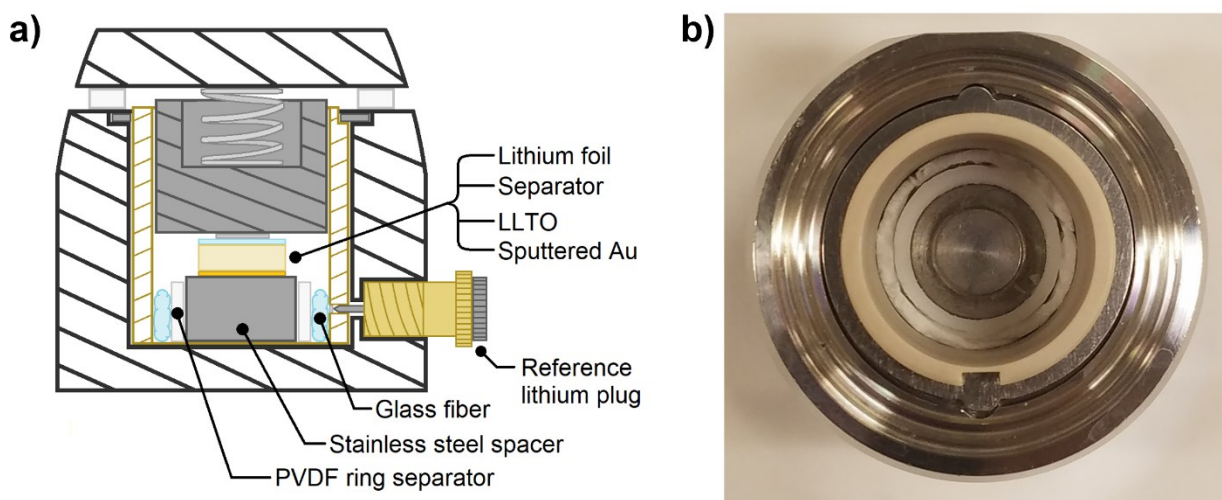


**Figure 2.** a) Diagram of three-electrode set-up, where the separator and glass fiber contain 1.0 M  $\text{LiPF}_6$  in EC/DEC = 50/50 (v/v) as liquid electrolyte. b) Top view of partially assembled test cell, showing the glass fiber, PVDF ring separator, and stainless-steel spacer.

### 3. Results and Discussion

#### 3.1 X-Ray Diffraction Analysis

The powder X-ray diffraction (XRD) patterns taken from a sample of each composition of the series  $\text{Li}_{0.33}\text{La}_{0.56}\text{Ti}_{1-x}\text{Se}_x\text{O}_3$  ( $x = 0, 0.025, 0.050, 0.075$ ) are presented together in Figure 3. These four compositions will be referred to as S00, S25, S50, and S75, respectively. All four compounds exhibit tetragonal lattice centering with a space group of  $P4/mmm$  at room temperature, matching with a previously reported diffraction pattern for tetragonal  $\text{Li}_{0.33}\text{La}_{0.56}\text{TiO}_3$  [15]. At lower nominal selenium content (S00, S25, and S50), only minor impurity peaks attributable to rutile  $\text{TiO}_2$  phase [16] are seen, likely from remaining precursor material. For S75, however, additional peaks appeared that could not be attributed to a precursor reagent ( $\text{La}_2\text{O}_3$ ,  $\text{TiO}_2$ ,  $\text{Li}_2\text{CO}_3$ ,  $\text{SeO}_2$ ) or a delithiated phase.

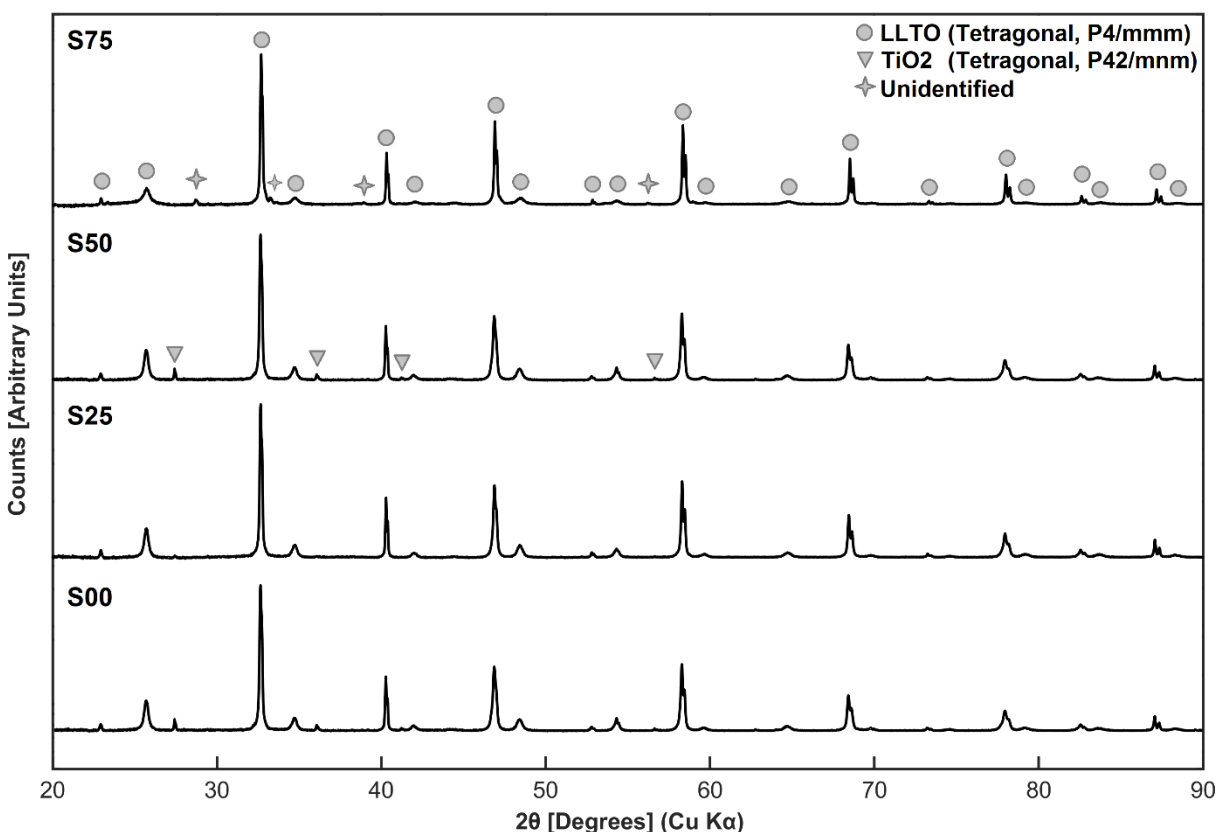


**Figure 3.** XRD patterns of  $\text{Li}_{0.33}\text{La}_{0.56}\text{Ti}_{1-x}\text{Se}_x\text{O}_3$  ( $x = 0, 0.025, 0.05, 0.075$ ), background subtracted. LLTO (tetragonal –  $P4/mmm$ ) peaks [15] are identified with circles, impurity peaks due to  $\text{TiO}_2$  (tetragonal –  $P42/mnm$ ) [16] are indicated with triangles, and new unprecedented peaks that appear at  $x = 0.075$  are identified with stars.

While the lack of any impurity peaks attributable to  $\text{SeO}_2$  might be an indication that suggests the LLTO had been successfully doped, it should be acknowledged that  $\text{SeO}_2$  has a boiling point of  $315^\circ\text{C}$  at atmospheric pressure [17]. Considering that the first-step of the synthesis procedure (calcination) required holding at  $1000^\circ\text{C}$  for 12 hours, it is possible that at least some of the  $\text{SeO}_2$  in the precursor mixture might have simply sublimed away. Analysis of XRD spectra does not necessarily provide information on the exact elemental composition of samples, especially for those without previously confirmed diffraction patterns; however, an indirect clue can be gleaned from the lattice parameters, which have been found to increase or decrease due to the substitution into the perovskite structure of dopants with different effective ionic radii [1]. The lattice constant values determined from Rietveld refinement of the XRD spectra obtained from the Se-doped samples is compared with that of the undoped sample in Table 1.

**Table 1.** Comparison of refined lattice constant values between LLTO samples of varying Se content ( $x = 0, 0.025, 0.05, \text{ and } 0.075$ )

Lattice Constant	S00	S25	S50	S75
a (Å)	3.873331	3.872449	3.872742	3.870763
b (Å)	3.874203	3.874254	3.873623	3.871733
c (Å)	7.760772	7.755625	7.767363	7.743892

The S75 sample exhibited lattice parameters that are consistently smaller than those of S00, which likely indicates successful doping as VI-coordinated  $\text{Se}^{4+}$  has a smaller effective ionic radius than VI-coordinated  $\text{Ti}^{4+}$  ( $0.50\text{\AA}$  vs.  $0.605\text{\AA}$ ) [10]. The same, however, cannot necessarily be said for the S25 and S50 samples, which exhibited inconsistent shrinking. When plotting the lattice parameters against nominal Se-content (Fig. 4), no consistent decreasing trend is seen when compared to the undoped sample. Although an overall consistent trend in lattice parameter changes as a function of dopant content is not always seen – such as in the case of  $\text{Ge}^{4+}$  or  $\text{Mn}^{4+}$  B-site doping [9] – the specific concern of  $\text{SeO}_2$  sublimation warrants further investigation into the elemental composition of synthesized samples. As such, while the emergence of new unidentified peaks for S75 (Fig. 3) could be an indication that the composition is approaching or is past the solubility limit of  $\text{Se}^{4+}$  substitution into  $\text{Li}_{0.33}\text{La}_{0.56}\text{TiO}_3$ , the exact value of that limit might not be specifically known from the present data.

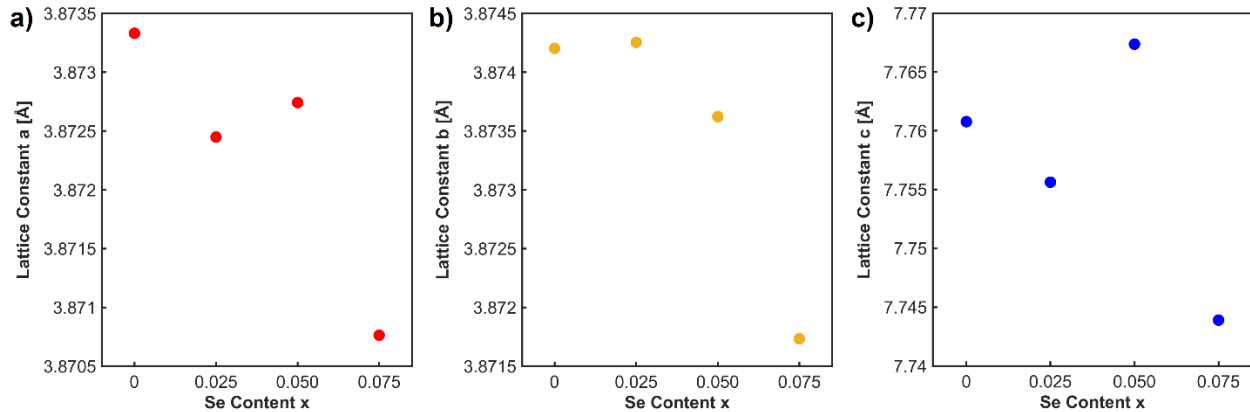


**Figure 4.** Lattice constant values **a)** a, **b)** b, and **c)** c obtained from XRD patterns of  $\text{Li}_{0.33}\text{La}_{0.56}\text{Ti}_{1-x}\text{Se}_x\text{O}_3$  ( $x = 0, 0.025, 0.05, 0.075$ ). While the S75 sample was found to have an overall decrease in lattice parameters compared to S00, no consistent decreasing trend is seen across the series of compositions.

### 3.2 Obtaining Bulk and Grain Boundary Conductivity Values

Complex impedance plots from potentiostatic electrochemical impedance spectroscopy (PEIS) experiments taken at room temperature (298.15 K) are shown in Figure 5. Similar to other LLTO studies [18], the spectra consists of three regions: a high frequency semi-circle around 1 MHz related to the bulk conductivity, a larger semi-circle spanning 100Hz to  $10^5$  Hz related to the grain boundary, and a low-frequency tail, which is often attributed to the lithium-blocking effect of the Au electrodes [11]. From a cursory visual inspection of the plots for the different compositions, it is notable that the spectra obtained for  $\text{Li}_{0.33}\text{La}_{0.56}\text{Ti}_{0.925}\text{Se}_{0.075}\text{O}_3$  (S75) features bulk and grain boundary semi-circles that are larger than those of the undoped LLTO sample while those of  $\text{Li}_{0.33}\text{La}_{0.56}\text{Ti}_{0.975}\text{Se}_{0.025}\text{O}_3$  (S25) and  $\text{Li}_{0.33}\text{La}_{0.56}\text{Ti}_{0.950}\text{Se}_{0.050}\text{O}_3$  (S50) are smaller. Although the exact composition of the synthesized pellets cannot be determined in the present study, the difference in behavior between S75, which is more likely to be Se-doped, and that of S25 and S50 could suggest that the S75 sample is past some sort of saturation limit for  $\text{Li}_{0.33}\text{La}_{0.56}\text{TiO}_3$ .

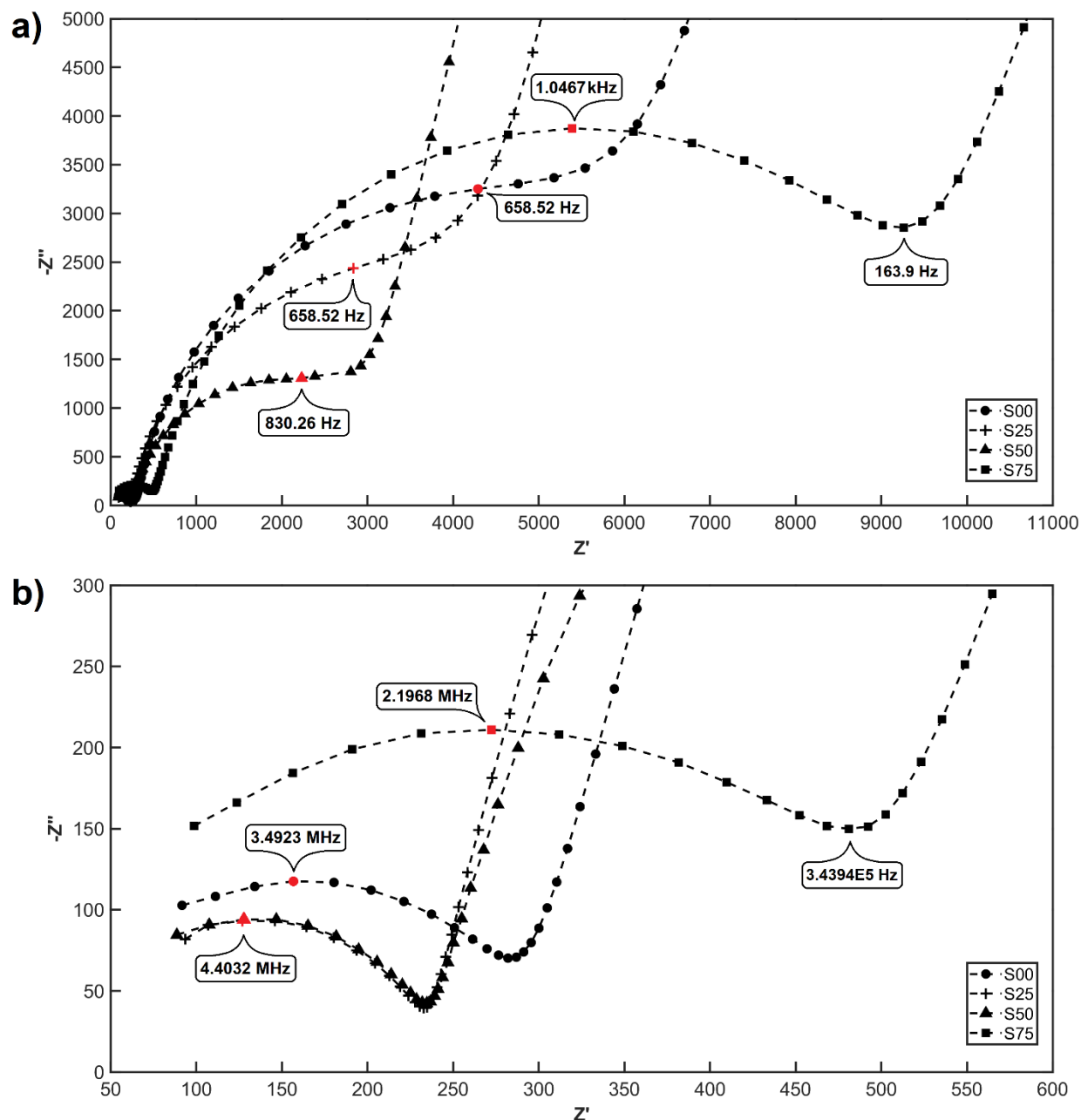


**Figure 5.** Comparison of room temperature complex impedance plots of the **a)** bulk and **b)** grain boundary semicircles for selenium doped LLTO samples.

Because the high-frequency semi-circle tended to shift to frequencies beyond the 1 MHz range of measurements at temperatures above room temperature (298.15K), values for grain boundary and bulk conductivities were extracted separately as shown in Figure 6 and Figure 7, respectively: the grain boundary from the 303.15K to 353.15K (high temperature) PEIS series and the bulk from the 263.15K to 298.15K (low temperature) PEIS series. The grain boundary conductivity was also extracted from the room temperature data.

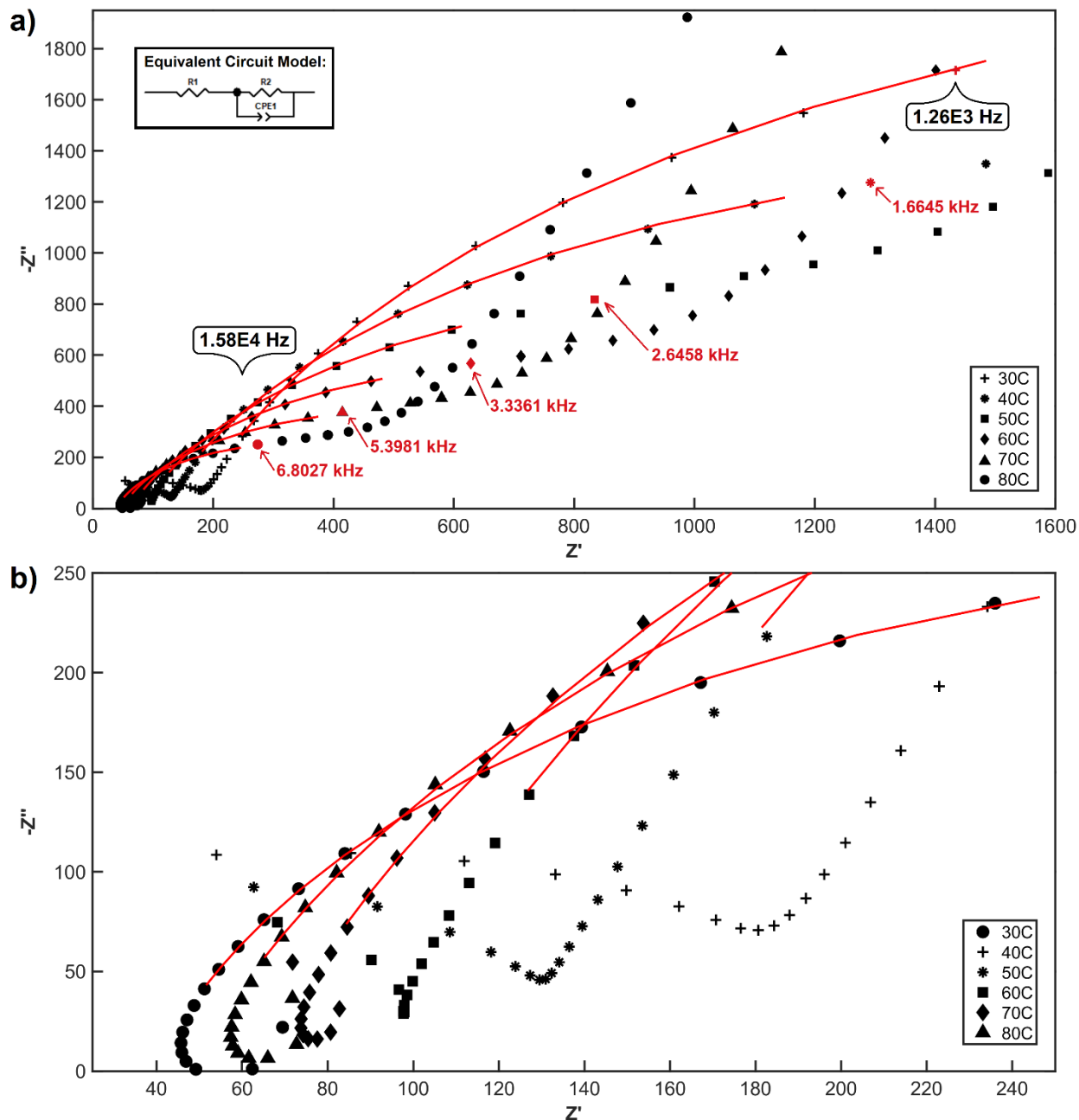


**Figure 6. a)** Representative image of semi-circle fitting (red lines) for high-temperature grain boundary conductivity impedance series of S25 sample, with frequency range of fitting for 30°C data indicated in boxes. **b)** High-frequency end of impedance data series (max freq. 1 MHz), showing partial or no bulk feature.



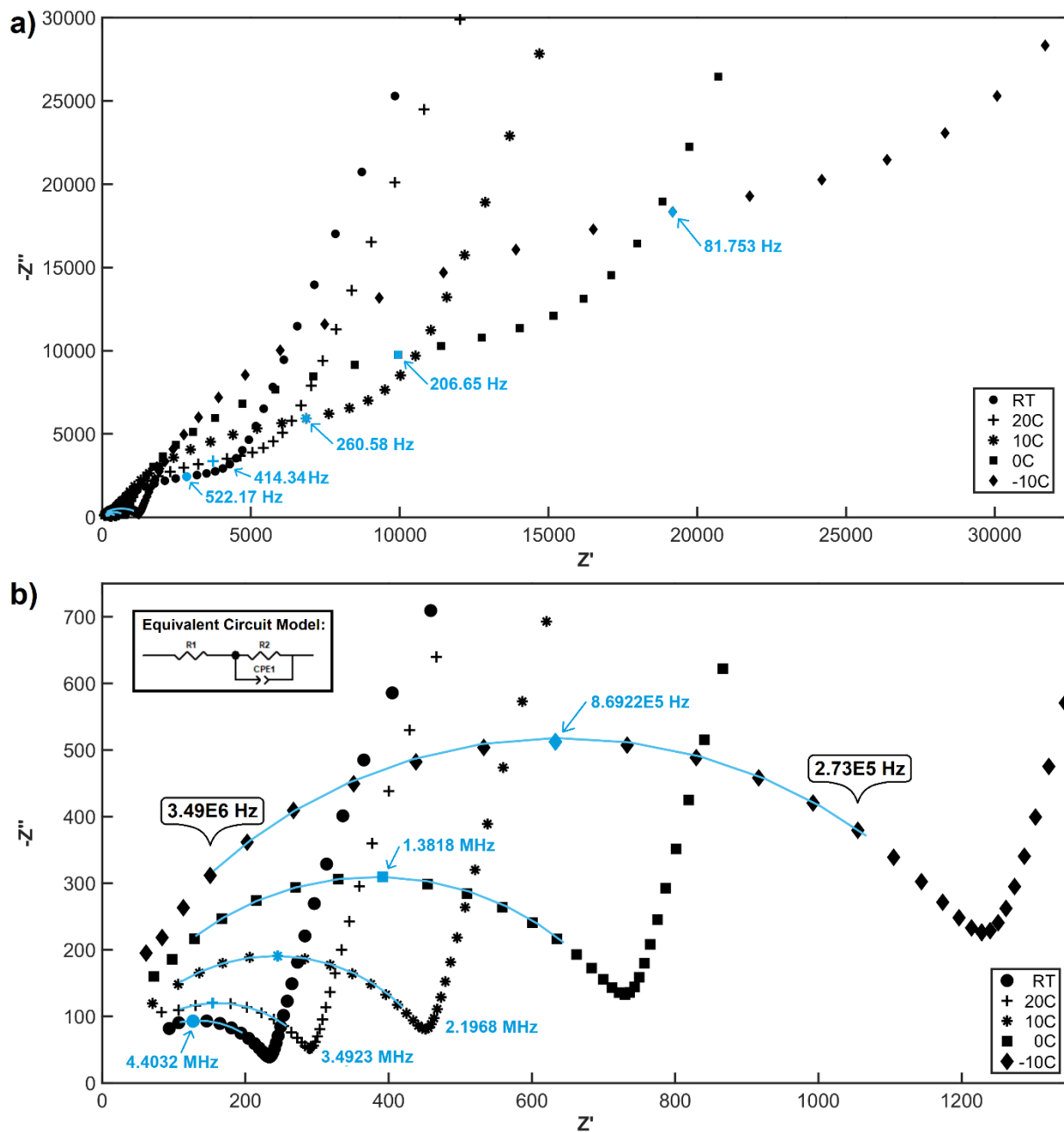


**Figure 7. a)** Grain boundary portion of low-temperature impedance data series of S25 sample. **b)** Representative image of semi-circle fitting (blue lines) of low-temperature data with frequency range of fitting for -10°C data indicated in boxes.

Bulk and grain boundary resistance values were then used with corresponding pellet dimensions (see Appendix A) to determine conductivity values according to the following equation:

$$\sigma = \frac{t}{R_2 A} \quad (1)$$

Arrhenius plots produced from bulk and grain boundary resistance values for the four Se-doped compositions (S00, S25, S50, and S75) are shown in Figure 8. From the resulting linear fits, values for activation energy were obtained and shown in Table 2 along with conductivity data. The activation energies are fairly comparable with each other, with a slight increase seen between S00 and some of the Se-doped compositions for bulk and grain boundary.

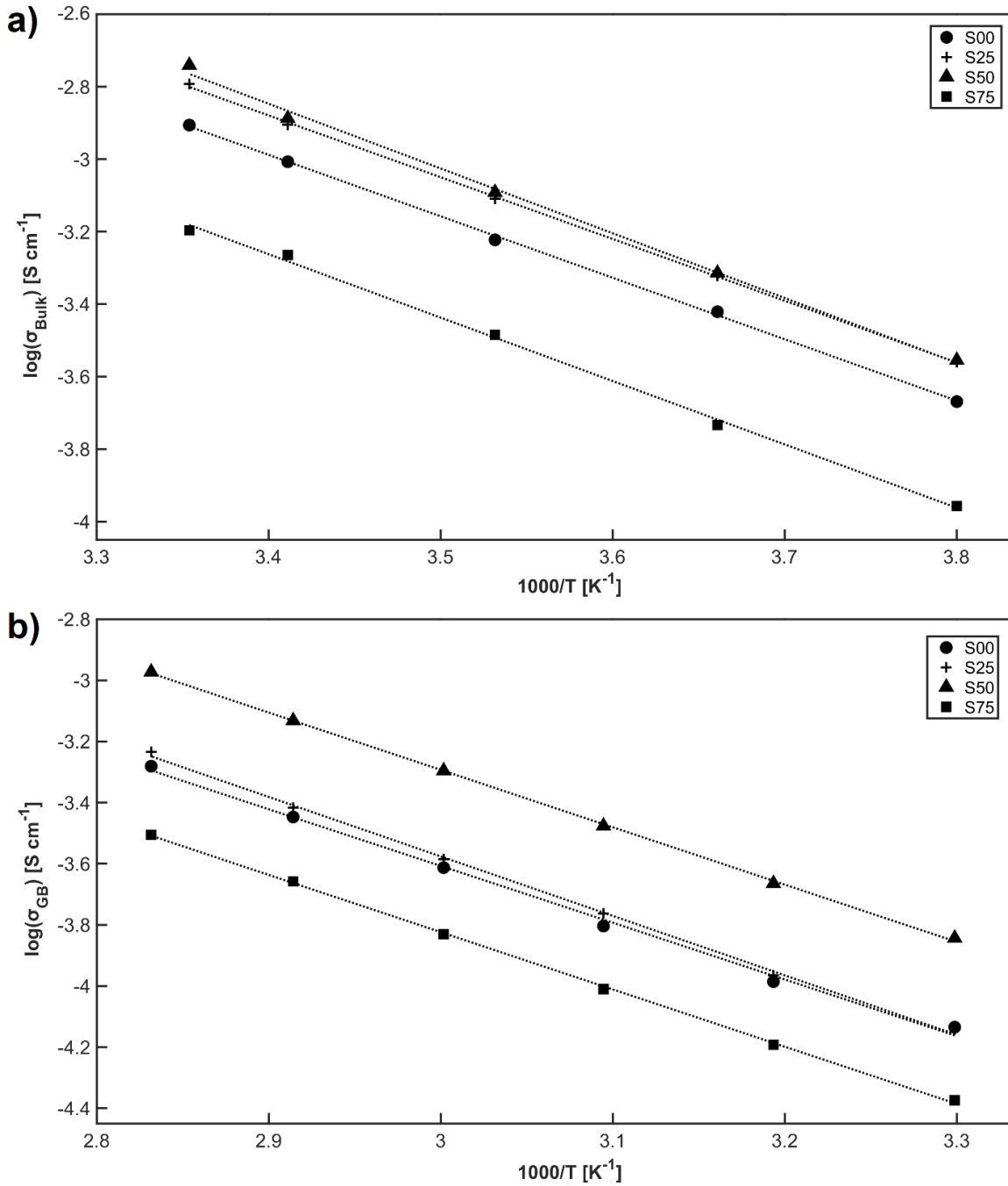


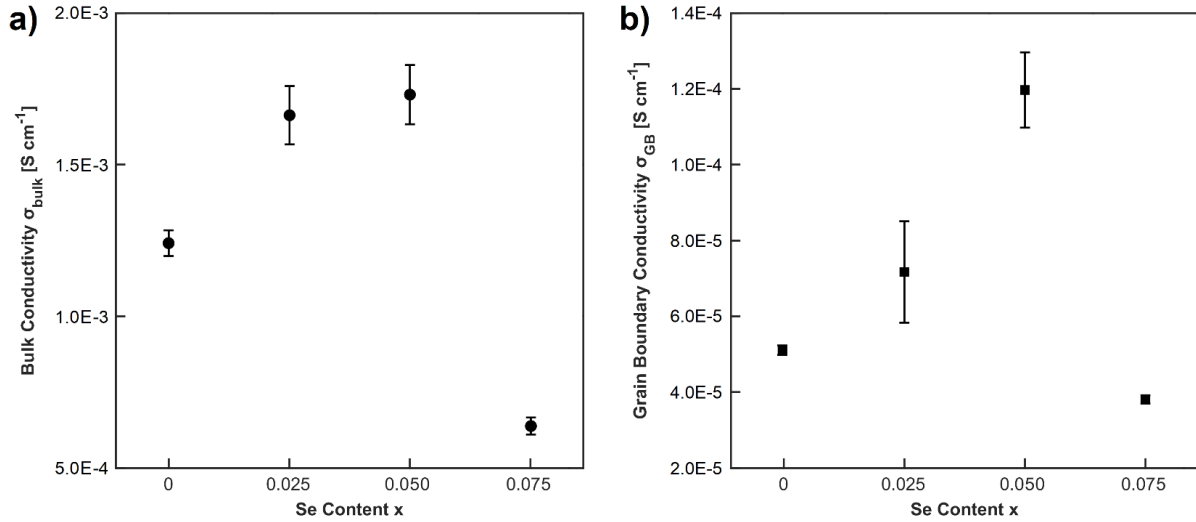
**Figure 8.** Arrhenius plots for the **a)** bulk conductivities and **b)** grain boundary conductivities

**Table 2.** Ionic conductivity data and activation energy data of Se-Doped LLTO

	S00	S25	S50	S75
$\sigma_{\text{bulk}}$ [S cm <sup>-1</sup> ]	$(1.24 \pm 0.04) \times 10^{-3}$	$(1.66 \pm 0.10) \times 10^{-3}$	$(1.73 \pm 0.10) \times 10^{-3}$	$(6.38 \pm 0.28) \times 10^{-4}$
$\sigma_{\text{GB}}$ [S cm <sup>-1</sup> ]	$(5.11 \pm 0.13) \times 10^{-5}$	$(7.17 \pm 1.34) \times 10^{-5}$	$(1.20 \pm 0.10) \times 10^{-4}$	$(3.81 \pm 0.11) \times 10^{-5}$
$E_{\text{bulk}}$ [eV]	$0.34 \pm 0.02$	$0.34 \pm 0.01$	$0.35 \pm 0.03$	$0.35 \pm 0.03$
$E_{\text{GB}}$ [eV]	$0.37 \pm 0.03$	$0.39 \pm 0.02$	$0.37 \pm 0.01$	$0.37 \pm 0.01$

### 3.3 Bulk and Grain Boundary Conductivity Comparison

Calculated values for room temperature bulk and grain boundary conductivity were plotted with error bars in Figure 9. Beginning with the bulk conductivity, the value obtained for undoped  $\text{Li}_{0.33}\text{La}_{0.56}\text{TiO}_3$  is  $(1.24 \pm 0.04) \times 10^{-3} \text{ S cm}^{-1}$ , which is larger but fairly close to previously reported values obtained from similar compositions of LLTO:  $\approx 1 \times 10^{-3} \text{ S cm}^{-1}$  for  $\text{Li}_{0.35}\text{La}_{0.55}\text{TiO}_3$  [19] and  $1.1 \times 10^{-3} \text{ S cm}^{-1}$  for  $\text{Li}_{0.3}\text{La}_{0.57}\text{TiO}_3$  [20]. As the  $x = 0.11$  member of the LLTO series is believed to exhibit the highest bulk ionic conductivity at room temperature, the larger bulk conductivity found here would appear to make sense. Looking then at the Se-doped pellets, the bulk conductivities of S25 and S50 appear to be larger than that of S00, at values of  $(1.66 \pm 0.10) \times 10^{-3} \text{ S cm}^{-1}$  and  $(1.73 \pm 0.10) \times 10^{-3} \text{ S cm}^{-1}$  respectively.

**Figure 9.** a) RT Bulk and b) grain boundary conductivity values for Se-doped LLTO

In the literature, comparable bulk conductivity can be seen with the B-site doping of  $\text{Al}^{3+}$ , with the composition  $(\text{Li}_{0.39}\text{La}_{0.54})_{1+y/2}\text{Al}_y\text{Ti}_{1-y}\text{O}_3$  ( $y = 0.02$ ) exhibiting a bulk conductivity of  $(1.58 \pm 0.01) \times 10^{-3} \text{ S cm}^{-1}$  at 300K [18]. Considering that VI-coordinated  $\text{Al}^{3+}$  has an effective ionic radius of  $0.535\text{\AA}$ , which is larger than the effective ionic radius of  $0.50\text{\AA}$  for VI-coordinated  $\text{Se}^{4+}$  [10], the results obtained here appear to agree with previous findings that suggested a link between B-site substitution of smaller cations with increased ionic conductivity due to the strengthening of the B-O bond [9]. Of course, the exact compositions of the Se-doped samples have yet to be determined, and there remains the question of the extent of Se-doping for S25 and S50 based on the inconsistent changes in the lattice parameters seen for these compositions. The decrease in bulk conductivity for S75 might be explained by the emergence of new phases seen in the XRD spectra (Fig. 3), as large amounts of substitution can lead to detrimental distortions in the B-site octahedra that impede lithium migration [9]. Again, however, because the exact composition of the nominally Se-doped samples is unknown, the actual maximum value for bulk conductivity and corresponding Se-content have yet to be determined.

As for the grain boundary conductivity, the room temperature value obtained for the undoped composition is in fairly good agreement with a previous finding for  $\text{La}_{0.57}\text{Li}_{0.29}\text{TiO}_3$ :  $4.68 \times 10^{-5} \text{ S cm}^{-1}$  at 303.15K [14] vs.  $(5.11 \pm 0.13) \times 10^{-5} \text{ S cm}^{-1}$  at 298.15K (this study). The increase in grain boundary conductivity for S25 and S50, however, is harder to explain with the current data at hand. Beyond questions about the Se-content of the pellets, grain boundary conductivity is often influenced by the synthesis process [1]. For example, it has been established that increased sintering temperatures can result in larger grain sizes, which reduces grain boundary regions and thus increases overall ionic conductivity [18]. While some variability would be expected because the preparation procedure involved hand-grinding with an agate mortar and pestle, there is still a statistically significant difference between the average grain boundary conductivities of S00 and that of S25 and S50. Although the sintering environment - specifically one with minimal moisture and carbon dioxide - has also been found to play a role in the presence of secondary phases and the quality of contact between grains [21], the samples prepared in this study had been synthesized under a flow of ultra-high purity oxygen (Airgas). Considering the grain boundary conductivity of  $7.36 \times 10^{-5} \text{ S cm}^{-1}$  reported for a sample of  $\text{Li}_{0.34}\text{La}_{0.55}\text{TiO}_3$  that had been sintered under flowing oxygen [21], the grain boundary value of  $(1.20 \pm 0.10) \times 10^{-4} \text{ S cm}^{-1}$  exhibited by S50 perhaps warrants investigation into the micro-structure after first confirming sample composition.

### 3.4 Stability of Se-Doped LLTO

Cyclic voltammograms (1.0V to 2.8V vs. Li) obtained from freshly assembled asymmetric cells (Au | LLTO | Separator | Li) for a pellet of nominal compositions S00 and S50 are shown in Figure 10. For the sake of clarity, the first cycle for the S00 pellet, which featured a large vertical artifact of the initialization process, has been omitted. Reduction occurs in both samples, but the onset appears to occur at a lower potential for S50 than S00.

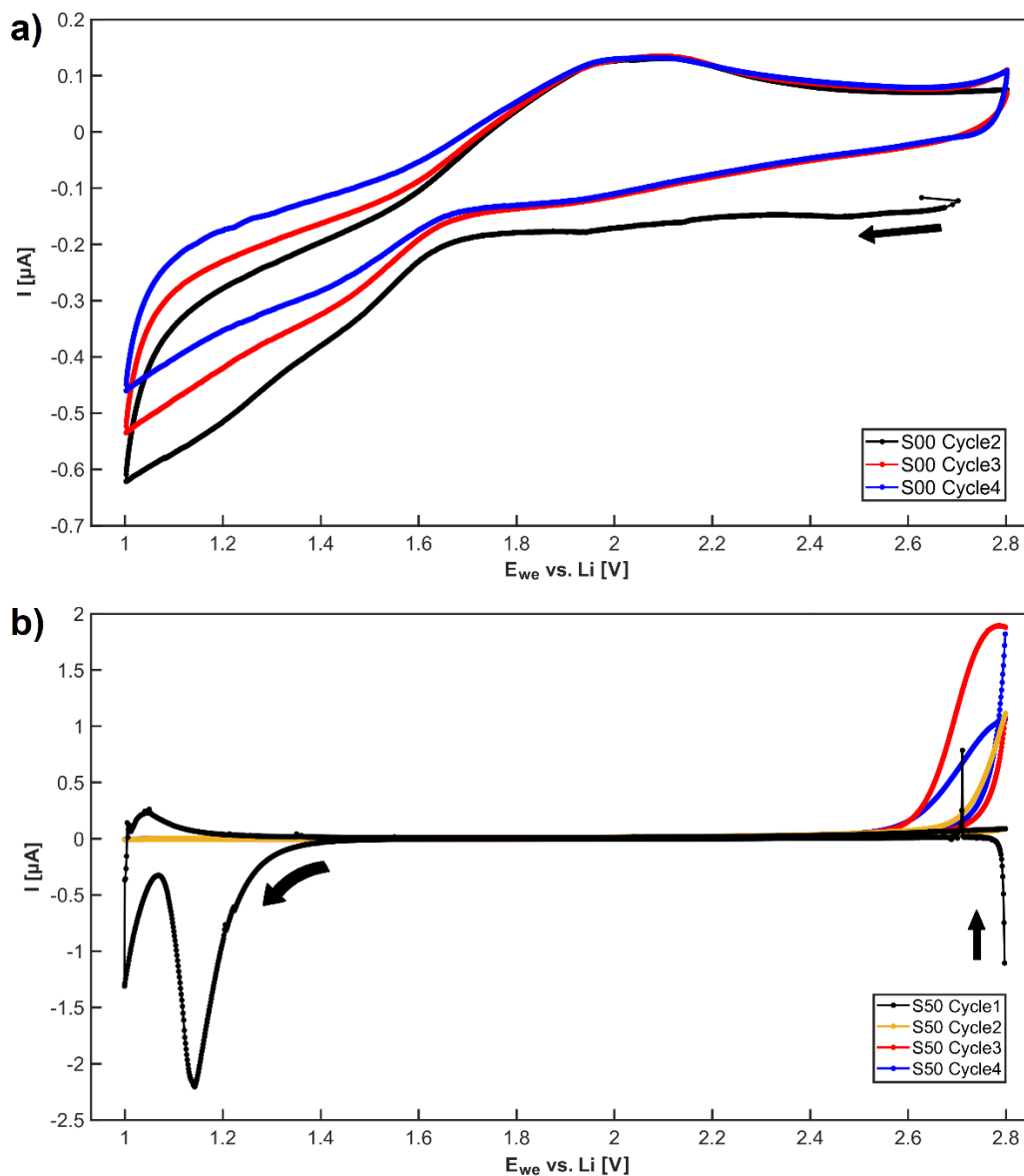


**Figure 10.** Voltammograms for pellet of composition **a)** S00 and **b)** S50 taken at scan rate of  $0.1 \text{ mV s}^{-1}$ . Sputtered Au as working electrode, lithium metal as counter separated from LLTO by membrane, and separate lithium metal as reference. Reduction occurs in both samples, but the onset appears to occur at a lower potential for S50 than S00.

In good agreement with the literature [1], the undoped LLTO began to be reduced at a potential around 1.7V vs. Li, which was also seen in the subsequent two cycles. Furthermore, the decreasing maximum value of the anodic current from Cycles 2 to 4 for S00 is likely indicative of lithium intercalation into the LLTO structure, an irreversible reaction that has been observed below potentials of 1.8V vs. Li [14]. This intercalation is the reason for the increased electronic conductivity of LLTO at such low potentials, which makes LLTO in its undoped form ill-suited as a solid-state electrolyte against very reducing anodes such as lithium metal.

Intercalation and, therefore, reduction also appear to occur in the Se-doped sample (S50). Notably, however, the onset of reduction in the first cycle appears to have occurred at a potential of around 1.4V vs. Li, which is lower than had been seen for the S00 sample. This result perhaps lends some credence to the potential of  $\text{Se}^{4+}$  B-site substitution to stabilize LLTO against a lithium metal anode. However, further refinement and investigation into stabilizing LLTO will necessitate first identifying the exact elemental compositions of nominally doped samples. It should also be noted that subsequent cycles of the S50 cell did not show any signs of reaction when sweeping down towards and back from 1V vs. Li. Previous studies had found the maximum amount of lithium intercalation into LLTO to be capped by the number of available A-sites in the perovskite structure [14]. Therefore, it would seem that the S50 sample rapidly reduced to full lithium intercalation capacity in only the first cycle, perhaps indicated by the appearance of the second peak at potentials closer to 1V vs. Li. The disparity in intercalation rate between the two samples, however, might be related to how well the separator used in the respective test cell assemblies kept the lithium metal foil from direct contact with the LLTO pellet: handling mistakes during the assembly process could have left small holes in the separator that allowed for direct contact.

Regardless, it should still be recognized that there is a membrane separator wetted with liquid electrolyte preventing direct contact between the LLTO pellet and lithium metal foil used as the counter electrode. As shown in figure 11, Se-doped LLTO pellets appear to readily reduced in contact with lithium metal, changing colors from cream to black as had been observed previously [5]. While the exact Se-content is currently unknown, it seems likely that nominal Se content of 2.5%, 5%, or 7.5% substitution is not enough to account for the large remaining amount  $\text{Ti}^{4+}$  content, which can readily reduce and increase the electrolyte's electronic conductivity. This is especially as precursor  $\text{SeO}_2$  could be sublimating away during the calcination process.



**Figure 11.** Picture of S50 sample pellet after accidental contact with a piece of lithium metal foil during the test cell assembly process in a glove box. Area of contact almost immediately changed color from cream to black.

## 4. Conclusion

Samples of nominal composition  $\text{Li}_{0.33}\text{La}_{0.56}\text{Ti}_{1-x}\text{Se}_x\text{O}_3$  ( $x = 0, 0.025, 0.050, 0.075$ ) were prepared using a two-step conventional synthesis method. Values for bulk and grain boundary conductivities were extracted along with associated activation energies from impedance data. From these results, the composition  $\text{Li}_{0.33}\text{La}_{0.56}\text{Ti}_{0.950}\text{Se}_{0.050}\text{O}_3$  (S50) was determined to have the largest conductivities at room temperature: bulk conductivity of  $(1.73 \pm 0.10) \times 10^{-3} \text{ S cm}^{-1}$  ( $E_{\text{Bulk}} = 0.35 \pm 0.03 \text{ eV}$ ) and grain boundary conductivity of  $(1.20 \pm 0.10) \times 10^{-4} \text{ S cm}^{-1}$  ( $E_{\text{GB}} = 0.37 \pm 0.01 \text{ eV}$ ). Initial stability measurements obtained using three-electrode cyclic voltammetry were also attempted, tentatively suggesting the possibility of LLTO stabilization against a Li metal anode through larger nominal Se-content substitution.

However, there remains uncertainty as to the exact composition and Se-content of the doped samples, particularly those of composition S25 and S50, for which inconsistent lattice parameter shrinking was determined from Rietveld refinement. While the apparent stability of the S50 sample down to 1.4V vs. Li is promising, elemental composition analysis is required to verify the success of and validate any claims about properties brought about through  $\text{Se}^{4+}$  B-site doping into the perovskite structure of LLTO.

If experiments to determine the composition of synthesized samples prove fruitful, investigations into the micro-structure and grain boundaries of Se-doped samples may be of interest to investigate potential mechanisms for the increase in grain boundary conductivity observed with samples of composition S25 and S50. Further work might also focus on pushing larger percentages of Se-substitution, especially for optimizing synthesis in light of potential  $\text{SeO}_2$  sublimation during calcination if a two-step conventional synthesis method is pursued. It might even be of interest to attempt a full replacement of  $\text{Ti}^{4+}$  for  $\text{Se}^{4+}$ , in a similar spirit to the lithium-rich perovskite  $\text{Li}_{1.5}\text{La}_{1.5}\text{TeO}_6$  [7], to understand possible trade-offs between stability and ionic conductivity for Se-doped LLTO.



## 5. References

- [1] Sun, Y., Guan, P., Liu, Y., Xu, H., Li, S., and Chu, D., 2019, “Recent Progress in Lithium Lanthanum Titanate Electrolyte towards All Solid-State Lithium Ion Secondary Battery,” *Critical Reviews in Solid State and Materials Sciences*, **44**(4), pp. 265–282.
- [2] Scrosati, B., and Garche, J., 2010, “Lithium Batteries: Status, Prospects and Future,” *Journal of Power Sources*, **195**(9), pp. 2419–2430.
- [3] Tarascon, J.-M., and Armand, M., 2001, “Issues and Challenges Facing Rechargeable Lithium Batteries,” *Nature*, **414**(6861), pp. 359–367.
- [4] Liu, B., Zhang, J.-G., and Xu, W., 2018, “Advancing Lithium Metal Batteries,” *Joule*, **2**(5), pp. 833–845.
- [5] Wang, M. J., Wolfenstine, J. B., and Sakamoto, J., 2020, “Mixed Electronic and Ionic Conduction Properties of Lithium Lanthanum Titanate,” *Advanced Functional Materials*, **30**(10), p. 1909140.
- [6] Bhuvanesh, N. S. P., and Gopalakrishnan, J., 1997, “Solid-State Chemistry of Early Transition-Metal Oxides Containing D0 and D1 Cations,” *J. Mater. Chem.*, **7**(12), pp. 2297–2306.
- [7] Amores, M., El-Shinawi, H., McClelland, I., Yeandel, S. R., Baker, P. J., Smith, R. I., Playford, H. Y., Goddard, P., Corr, S. A., and Cussen, E. J., 2020, “Li<sub>1.5</sub>La<sub>1.5</sub>MO<sub>6</sub> (M = W<sup>6+</sup>, Te<sup>6+</sup>) as a New Series of Lithium-Rich Double Perovskites for All-Solid-State Lithium-Ion Batteries,” *Nat Commun*, **11**(1), p. 6392.
- [8] Nazri, G.-A., and Pistoia, G., eds., 2009, *Lithium Batteries: Science and Technology*, Springer, New York, NY.
- [9] Chung, H.-T., Kim, J.-G., and Kim, H.-G., 1998, “Dependence of the Lithium Ionic Conductivity on the B-Site Ion Substitution in (Li<sub>0.5</sub>La<sub>0.5</sub>)Ti<sub>1-x</sub>M<sub>x</sub>O<sub>3</sub> (M=Sn, Zr, Mn, Ge),” *Solid State Ionics*, **107**(1), pp. 153–160.
- [10] Shannon, R. D., 1976, “Revised Effective Ionic Radii and Systematic Studies of Interatomic Distances in Halides and Chalcogenides,” *Acta Cryst A*, **32**(5), pp. 751–767.
- [11] Stramare, S., Thangadurai, V., and Weppner, W., 2003, “Lithium Lanthanum Titanates: A Review,” *Chem. Mater.*, **15**(21), pp. 3974–3990.
- [12] Chandra, S., Kim, Y., Vivona, D., Waluyo, I., Hunt, A., Schlueter, C., Lee, J. B., Shao-Horn, Y., and Yildiz, B., 2022, “Thermally-Driven Reactivity of Li<sub>0.35</sub>La<sub>0.55</sub>TiO<sub>3</sub> Solid Electrolyte with LiCoO<sub>2</sub> Cathode,” *J. Mater. Chem. A*, **10**(7), pp. 3485–3494.
- [13] Bohnke, O., Emery, J., and Fourquet, J.-L., 2003, “Anomalies in Li<sup>+</sup> Ion Dynamics Observed by Impedance Spectroscopy and <sup>7</sup>Li NMR in the Perovskite Fast Ion Conductor (Li<sub>3x</sub>La<sub>2/3-x</sub>□<sub>1/3-2x</sub>)TiO<sub>3</sub>,” *Solid State Ionics*, **158**(1), pp. 119–132.
- [14] Chen, C. H., and Amine, K., 2001, “Ionic Conductivity, Lithium Insertion and Extraction of Lanthanum Lithium Titanate,” *Solid State Ionics*, **144**(1), pp. 51–57.
- [15] Fourquet, J. L., Duroy, H., and Crosnier-Lopez, M. P., 1996, “Structural and Microstructural Studies of the Series La<sub>2/3-x</sub>Li<sub>3x</sub>□<sub>1/3-2x</sub>TiO<sub>3</sub>,” *Journal of Solid State Chemistry*, **127**(2), pp. 283–294.
- [16] Baur, W. H., and Khan, A. A., 1971, “Rutile-Type Compounds. IV. SiO<sub>2</sub>, GeO<sub>2</sub> and a Comparison with Other Rutile-Type Structures,” *Acta Cryst B*, **27**(11), pp. 2133–2139.
- [17] National Center for Biotechnology Information, 20233, “PubChem Compound Summary for CID 24007, Selenium Dioxide,” PubChem [Online]. Available: <https://pubchem.ncbi.nlm.nih.gov/compound/24007>. [Accessed: 09-May-2023].

- [18] He, L. X., and Yoo, H. I., 2003, "Effects of B-Site Ion (M) Substitution on the Ionic Conductivity of  $(\text{Li}_{3x}\text{La}_{2/3-x})_{1+y/2}(\text{MyTi}_{1-y})\text{O}_3$  (M=Al, Cr)," *Electrochimica Acta*, **48**(10), pp. 1357–1366.
- [19] Inaguma, Y., Chen, L., Itoh, M., and Nakamura, T., 1994, "Candidate Compounds with Perovskite Structure for High Lithium Ionic Conductivity," *Solid State Ionics*, **70–71**, pp. 196–202.
- [20] Kawai, H., and Kuwano, J., 1994, "Lithium Ion Conductivity of A-Site Deficient Perovskite Solid Solution  $\text{La}_{0.67-x}\text{Li}_{3x}\text{TiO}_3$ ," *J. Electrochem. Soc.*, **141**(7), p. L78.
- [21] Aguesse, F., López Del Amo, J. M., Roddatis, V., Aguadero, A., and Kilner, J. A., 2014, "Enhancement of the Grain Boundary Conductivity in Ceramic  $\text{Li}_{0.34}\text{La}_{0.55}\text{TiO}_3$  Electrolytes in a Moisture-Free Processing Environment," *Adv. Mater. Interfaces*, **1**(7), p. 1300143.

## 6. Appendices

### *Appendix A*

**Table 3.** Dimensions of sintered Se-doped LLTO pellets used for impedance spectroscopy measurements (measured using digital calipers)

	<b>S00_1 (Pure)</b>	<b>S00_2 (Pure)</b>	<b>S25_1 (<math>x=0.25</math>)</b>	<b>S25_2 (<math>x=0.25</math>)</b>	<b>S50_1 (<math>x=0.50</math>)</b>	<b>S50_2 (<math>x=0.50</math>)</b>	<b>S75_1 (<math>x=0.75</math>)</b>	<b>S75_2 (<math>x=0.75</math>)</b>
<b>Diameter [cm]</b>	0.893 $\pm 0.002$	0.895 $\pm 0.003$	0.906 $\pm 0.004$	0.909 $\pm 0.009$	0.892 $\pm 0.003$	0.891 $\pm 0.004$	0.911 $\pm 0.004$	0.911 $\pm 0.004$
<b>Thickness [cm]</b>	0.145 $\pm 0.005$	0.153 $\pm 0.004$	0.155 $\pm 0.006$	0.155 $\pm 0.001$	0.145 $\pm 0.003$	0.154 $\pm 0.004$	0.154 $\pm 0.003$	0.159 $\pm 0.002$